Project Report
LSP-283

Valleytronic Logic Gate: FY19 Advanced Devices Line-Supported Program

S.A. Vitale

27 January 2020

Lincoln Laboratory
MASSACHUSETTS INSTITUTE OF TECHNOLOGY
LEXINGTON, MASSACHUSETTS

This material is based upon work supported by the Under Secretary of Defense for Research and Engineering under Air Force Contract No. FA8702-15-D-0001.

This report is the result of studies performed at Lincoln Laboratory, a federally funded research and development center operated by Massachusetts Institute of Technology. This material is based upon work supported under Air Force Contract No. FA8702-15-D-0001. Any opinions, findings, conclusions or recommendations expressed in this material are those of the author(s) and do not necessarily reflect the views of the Under Secretary of Defense for Research and Engineering.

Massachusetts Institute of Technology
Lincoln Laboratory

Valleytronic Logic Gate: FY19 Advanced Devices Line-Supported Program

S.A. Vitale
Group 81

Project Report LSP-283
27 January 2020

Lexington Massachusetts

ABSTRACT

Classical computing faces a significant challenge. Field effect transistor technology is reaching the fundamental limits of scaling and no proposed replacement technology has yet demonstrated even comparable performance. A transformational device based on new physical phenomena could provide a new route to continued improvement in microelectronic power and performance. Two-dimensional transition metal dichalcogenides (TMDs) possess a number of intriguing electronic, photonic, and excitonic properties. This proposal focuses on their Valleytronic properties, which are truly unique to this new class of materials. Due to a lack of inversion symmetry and strong spin-orbit coupling, 2D TMDs possess individually addressable valleys in momentum space at the K and K' points in the first Brillouin zone. This valley addressability opens the possibility of using electron and hole momentum states as a completely new paradigm in information processing. Manipulating the K and K' momentum states could permit classical computation at a small fraction of the energy cost incurred by traditional field effect transistors.

The Valleytronic Logic Gate Line program began to explore the viability of creating a classical logic gate which would provide a PPA (power, performance, area) advantage over silicon CMOS. It was not within the scope of funding to build a logic gate and test it experimentally. Instead, some basic valleytronic material parameters were measured and using that information an analysis was performed of the power and speed of a notional gate design. Section 1 provides an introduction to valleytronic principles, Section 2 describes the measurements, Section 3 describes the performance projections, Section 4 summarizes the results of the project and Section 5 lists references and Lincoln and MIT external presentations from this work in FY19.

TABLE OF CONTENTS

LIST OF ILLUSTRATIONS

1. INTRODUCTION TO VALLEYTRONICS

This section is largely reproduced from a recent publication by Vitale et al [1].

When atoms brought together in close proximity form a crystal, the electrons of the constituent atoms interact with each other and with the atoms themselves, giving rise to distinct bands of energy that determine the electronic properties of the crystalline material. In semiconducting crystals, the bonding electrons populate a filled band of allowed states known as the valence band, and are separated from an unfilled band of higher energy known as the conduction band by an energy gap that contains no allowed states (the band gap). For some semiconductors, regions of minimum energy can appear in the conduction band that are indistinguishable from one another except for the direction of the crystal axes along which the energy band is oriented. Therefore, when carriers are excited across the band gap from the valence band into these minima in the conduction band, they will possess the same energy (be energy degenerate), but will have differing crystal momenta depending on the orientations of the axes. We refer to these minima as valleys, and to devices exploiting the fact that electrons, holes, or excitons (hereafter particles) are present in one valley vs. another as valleytronic devices. Selectively populating one momentum-distinguishable valley vs. another—creating a valley polarization—is the key enabling feature of valleytronics.

The localization of a particle to a region of momentum space yields a new index by which to characterize it, namely, the valley pseudospin. This is in addition to the discrete spin index normally associated with a particle. Though energy-degenerate valleys are present in many periodic solids, it is usually impossible to address or manipulate particles in one valley independently from another as the valley state of a particle does not strongly couple to an applied external force. Therefore, it is impractical to construct useful valleytronic devices out of most materials. This is in contrast to spintronics, for example, where the electron spin is readily manipulated by magnetic fields through the electron spin magnetic moment or (less easily) by electric fields through spin-orbit coupling. For valleytronics to be useful, it is also of paramount importance that the particles populating a valley reside there for long enough to perform a desired function.

In some materials, anisotropy of the particle mass along different crystal orientations can result in valley polarization under an applied field; preferential scattering occurs from one valley to another. This has been shown in diamond, aluminum arsenide, silicon, and bismuth at cryogenic temperatures. However, these materials still lack a strong coupling between the valley index and an external field. It is not possible to selectively initialize, manipulate, and read out particles in a specific valley, so we do not consider these materials in our discussion of valleytronics.

Fortunately, a class of materials does exist in which the valley pseudospin can be more readily addressed. In stark contrast to all other materials, 2D materials such as graphene and monolayer molybdenum disulfide possess valleys at the inequivalent K and K' points in the Brillouin zone (Figure 1), which exhibit strong valley-selective interactions with applied electric and magnetic fields. The isolation

and investigation of these materials were seminal events in the field of valleytronics. As one can see in the histogram of publications in the field in Figure 2, the isolation of graphene in 2004 catalyzed new research in valley physics, but investigations into the optical properties of transition metal dichalcogenide (TMD) monolayers in 2010 caused an explosion in the number of valleytronic publications.

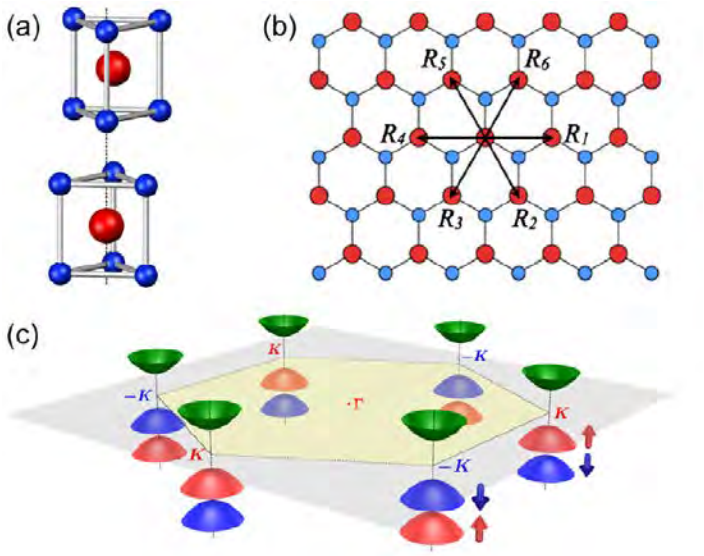

Figure 1. TMD crystal structure and Brillouin zone. From [2].

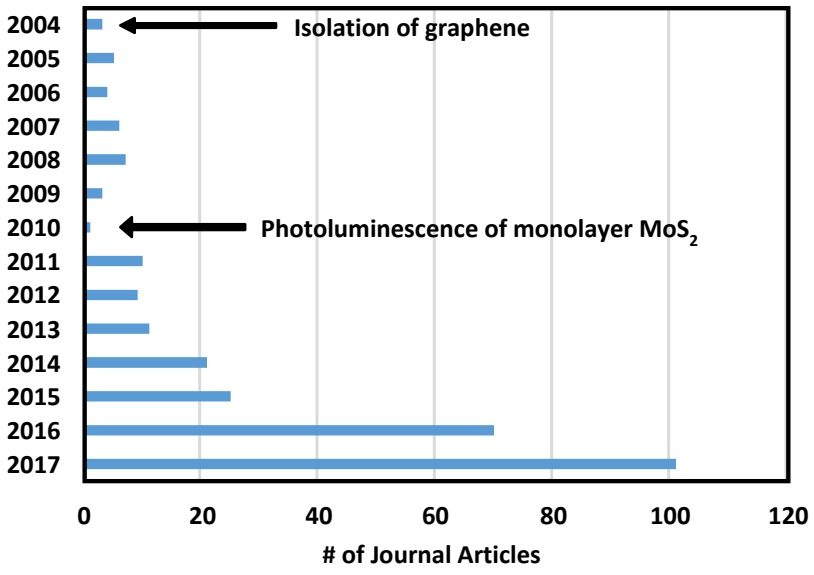

Figure 2. Number of relevant publications per year with "Valley" or "Valleytronic" in the title from the Compendex and Inspec databases.

The following discussion explains why some fundamental symmetries of monolayer materials are critical to valley addressability; it is largely based on published work in references [3–5]. We first elaborate on these symmetries and some valley-related concepts to clarify them for the reader.

In order to selectively couple to distinct valley states, it is necessary that there exist physical quantities that can distinguish between them. One such quantity is the Berry curvature, $\boldsymbol{\Omega}$**.** The Berry curvature describes the geometric properties of the electronic bands, and is central to the understanding of band topology-related effects. When describing the motion of electrons in crystal lattices, the semiclassical equations of motion are typically used, in which an electron is treated as a Bloch wave that can propagate through the crystal and the mean velocity is proportional to the gradient of the electronic energy of the band. The periodicity of the lattice is taken into account (by the Bloch form of the electron wavefunction), as well as the response of the carriers to applied electric and magnetic fields. However, an additional contribution exists that is sometimes ignored—an anomalous velocity can appear that is proportional to the Berry curvature of an electronic band and is established transverse to the applied electric field. This is of fundamental importance, as it can allow valley currents and related phenomena to manifest in materials with non-vanishing Berry curvature.

Another physical quantity that can be used to distinguish valley states is the orbital magnetic moment, $\boldsymbol{m}$. Intuitively, it can be regarded as due to the self-rotation of an electron wavepacket. It is particularly useful since one can use it to discriminate between valley states in ways similar to experiments that exploit the spin magnetic moment of a charge carrier (for example, a magnetic field can differentiate between spin up and spin down states since they have opposite magnetic moments). The Berry curvature and orbital magnetic moment and one's ability to use them to distinguish valley states can vanish, however, if two types of symmetry simultaneously exist in a crystal—time-reversal symmetry and inversion symmetry.

In general, time-reversal symmetry refers to the symmetry of a system under a reversal of the sign of the time, whereas spatial inversion symmetry refers to symmetry under a reversal of the direction of all the coordinate axes. These simple symmetries have far-reaching consequences. Pseudovectors such as the Berry curvature and the orbital magnetic moment do not change sign under spatial inversion. Therefore, one cannot use a pseudovector such as the Berry curvature to distinguish between valleys if inversion symmetry and time-reversal symmetry are simultaneously present, as it would vanish identically. The K and K' points in hexagonal 2D materials are time-reversed images of one another, so in general, physical qualities that have odd parity under time reversal are good candidates to distinguish valley states. If the Berry curvature and orbital magnetic moment are non-equivalent at the K and K' points, one can, in principle, distinguish between the valleys using electric and magnetic fields, respectively. This is shown below.

The semiclassical equations of motion for Bloch electrons under applied electric and magnetic fields with non-vanishing Berry curvature are

$$\dot{\boldsymbol{r}} = \frac{1}{\hbar}\frac{\partial E_n(\boldsymbol{k})}{\partial \boldsymbol{k}} - \dot{\boldsymbol{k}} \times \Omega_n(\boldsymbol{k})$$

$$\hbar\dot{\boldsymbol{k}} = -e\boldsymbol{E} - e\dot{\boldsymbol{r}} \times \boldsymbol{B}$$

where $\boldsymbol{\Omega}$ can be defined in terms of the Bloch functions:

$$\boldsymbol{\Omega_n}(\boldsymbol{k}) = \nabla_{\boldsymbol{k}} \times A_n(\boldsymbol{k})$$

$$A_n(\boldsymbol{k}) = i \int u_n^* (\boldsymbol{r}, \boldsymbol{k})\, \nabla_{\boldsymbol{k}} u_n(\boldsymbol{r}, \boldsymbol{k})\, d^3\boldsymbol{r}$$

A_n is the Berry connection and u_n is the periodic part of the Bloch electron wavefunction in the nth energy band. The Berry curvature can also be written as

$$\boldsymbol{\Omega}_n(\boldsymbol{k}) = i\frac{\hbar^2}{m^2}\sum_{i\neq n}\frac{\boldsymbol{P}_{n,i}(\boldsymbol{k}) \times \boldsymbol{P}_{i,n}(\boldsymbol{k})}{\left[E_n^0(\boldsymbol{k}) - E_i^0(\boldsymbol{k})\right]^2}$$

where $E_n^0(\boldsymbol{k})$ is the energy dispersion of the nth band and $\boldsymbol{P}_{n,i}(\boldsymbol{k}) = \langle u_n|v|u_i\rangle$ is the matrix element of the velocity operator. By demanding that the equation of motion must remain invariant under the system symmetry, one can see that with time-reversal symmetry, $\boldsymbol{\Omega}_n(\boldsymbol{k}) = -\boldsymbol{\Omega}_n(-\boldsymbol{k})$, and with inversion symmetry $\boldsymbol{\Omega}_n(\boldsymbol{k}) = \boldsymbol{\Omega}_n(-\boldsymbol{k})$. Thus, only when inversion symmetry is broken can valley-contrasting phenomena manifest. From the equations of motion, we see that if an in-plane electric field is applied in a 2D crystal, then a non-zero Berry curvature results in an anomalous electron velocity perpendicular to the field, and the velocity would have opposite sign for electrons in opposite valleys.

The broken inversion symmetry also allows the existence of the orbital magnetic moment. The electron energy dispersion in the nth band is modified to

$$E_n(\boldsymbol{k}) = E_n^0(\boldsymbol{k}) - \boldsymbol{m_n}(\boldsymbol{k}) \cdot \boldsymbol{B}$$

where the quantity $\boldsymbol{m}$ is the orbital magnetic moment, given by

$$\boldsymbol{m}(\boldsymbol{k}) = i\frac{e\hbar}{2m^2}\sum_{i\neq n}\frac{\boldsymbol{P}_{n,i}(\boldsymbol{k}) \times \boldsymbol{P}_{i,n}(\boldsymbol{k})}{E_n^0(\boldsymbol{k}) - E_i^0(\boldsymbol{k})}$$

Finite $\boldsymbol{m}$ is responsible for the anomalous g factor of electrons in semiconductors, which manifests itself in a shift of Zeeman energy in the presence of a magnetic field.

The existence of finite orbital magnetic moment also suggests that the valley carriers will possess optical circular dichroism, i.e., they will exhibit different properties upon illumination with right- or left-circularly polarized light [6–8]. Though optical circular dichroism is also present in systems with broken time-reversal symmetry, it should be understood that the underlying physics in valleytronic materials is quite different and the dichroism is present even when time-reversal symmetry is maintained. One effect of the orbital magnetic moment is valley optical selection rules. [4]

As a specific example, the 2H phase of many 2D transition metal dichalcogenides lack inversion symmetry and, as a result, exhibit contrasting $\boldsymbol{\Omega}$ and $\boldsymbol{m}$ between the K and K' valleys. The $\boldsymbol{k}\cdot\boldsymbol{p}$ Hamiltonian at the band edges in the vicinity of K and K' is given by

$$\widehat{H} = at\left(\tau_z k_x \sigma_x + k_y \sigma_y\right) + \frac{\Delta}{2}\sigma_z$$

where a is the lattice spacing, t is the nearest neighbor hopping integral, $\tau_z = \pm 1$ is the valley index, σ is the Pauli matrix element, and Δ is the band gap. In this case, the Berry curvature in the conduction band is given by

$$\boldsymbol{\Omega}_c(k) = -\hat{\boldsymbol{z}}\frac{2a^2t^2\Delta}{(4a^2t^2k^2+\Delta^2)^{3/2}}\tau_z$$

Because of the finite Berry curvature with opposite signs in the two valleys, an in-plane electric field induces a Valley Hall Effect for the carriers (Figure 3). Note that the Berry curvature in the valence band is equal to that in the conduction band, but with opposite sign.

The orbital magnetic moment has identical values in the valence and conduction bands:

$$\boldsymbol{m}(k) = -\hat{\boldsymbol{z}}\frac{2a^2t^2\Delta}{4a^2t^2k^2+\Delta^2}\frac{e}{2\hbar}\tau_z$$

Non-zero $\boldsymbol{m}$ implies that the valleys have contrasting magnetic moments (through $\tau_z = \pm 1$) and therefore it is possible to detect valley polarization through a magnetic signature. The orbital magnetic moment also gives rise to the circularly polarized optical selection rules for interband transitions. The Berry curvature, orbital magnetic moment, and optical circular dichroism $\eta(\boldsymbol{k})$ are related by

$$\eta(\boldsymbol{k}) = -\frac{\boldsymbol{m}(\boldsymbol{k})\cdot\hat{\boldsymbol{z}}}{\mu_B^*(\boldsymbol{k})} = -\frac{\boldsymbol{\Omega}(\boldsymbol{k})\cdot\hat{\boldsymbol{z}}}{\mu_B^*(\boldsymbol{k})}\frac{e}{2\hbar}\Delta(\boldsymbol{k})$$

where $\mu_B^* = e\hbar/2m^*$ and $\Delta(\boldsymbol{k}) = (4a^2t^2k^2+\Delta^2)^{1/2}$ is the direct transition energy, or band gap, at $\mathbf{k}$. At the energetic minima of the K and K' points, we have full selectivity with $(\boldsymbol{k}) = -\tau_z$. The transition at K couples only to σ^+ light and the transition at K' couples only to σ^-. This selectivity allows the optical preparation, control, and detection of valley polarization (Figure 4).

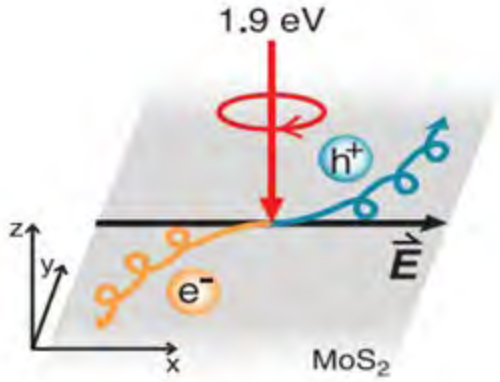

Figure 3. Anomalous motion perpendicular to an applied magnetic field (Valley Hall Effect) caused by finite and contrasting Berry curvature. From [9].

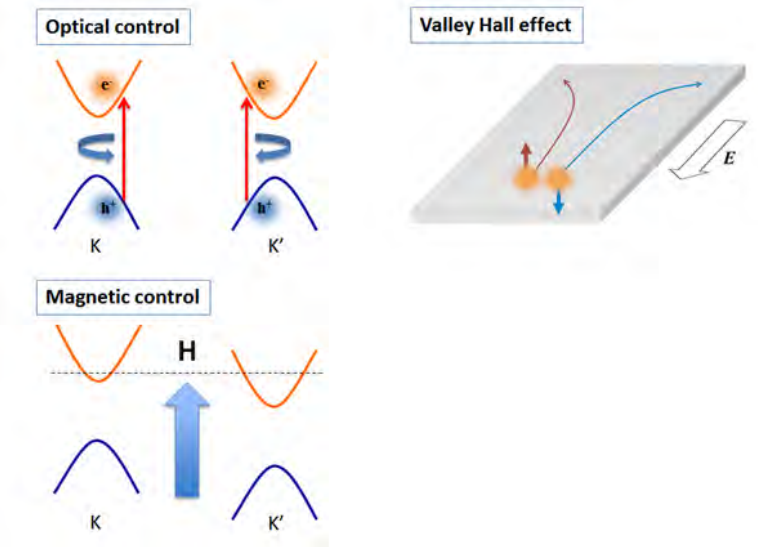

Figure 4. Three methods of control of the valley state: optical, electrostatic, and magnetic. Courtesy Kin Fai Mak, from the 2017 Valleytronics Workshop.

In summary, if the Berry curvature has different values at the K and K' points, one can expect different particle behavior in each valley as a function of an applied electric field. If the orbital magnetic moment has different values at the K and K' points, one can expect different behavior in each valley as a function of an applied magnetic field. Contrasting values of $\boldsymbol{\Omega}$ and $\boldsymbol{m}$ at the K and K' points give rise to optical circular

dichroism between the two valleys, which allows selective excitation of photons with right- or left-helicity. In order to have contrasting values of $\boldsymbol{\Omega}$ and $\boldsymbol{m}$ while maintaining time reversal symmetry, it is necessary that the material exhibit a lack of spatial inversion symmetry. Though spatial inversion symmetry can be induced in gapped graphene, by biasing the substrate underlying bilayer graphene, for example, monolayer 2D transition metal dichalcogenides meet this requirement without the need to externally introduce a band gap or symmetry breaking, and therefore TMDs appear to be the most promising candidates for useful valleytronic applications.

This page intentionally left blank.

2. VALLEYTRONIC MATERIALS MEASUREMENTS

2.1 VALLEY LIFETIME

To perform a useful function, valley-based phenomena must persist over timescales long enough to complete a computational transaction. In this section, we assess valley lifetime through time-resolved measurements performed by Nuh Gedik's group at in the MIT Department of Physics. Valley lifetime is here interpreted to mean how long a particle rests in one valley, say K, before scattering to the opposite valley.

The experimental setup is shown in Figure 5. A circularly polarized probe beam tuned to the WS2 A exciton resonance is continuously monitored to measure the reflectivity of the sample. A circularly polarized sub-band-gap pump beam creates a valley-selective population of excitons. The sub-band-gap excitation is effective due to the optical Stark effect, which will not be described on detail here. When the pump and probe are co-circularly polarized, a significant change in reflection occurs (Figure 6); when they are cross-circularly polarized, no change in reflectance is observed. The decay in the co-circularly polarized reflectance signal is a measure of valley polarization lifetime. For this ML WS_2 sample, the valley lifetime is approximately 0.2 ps.

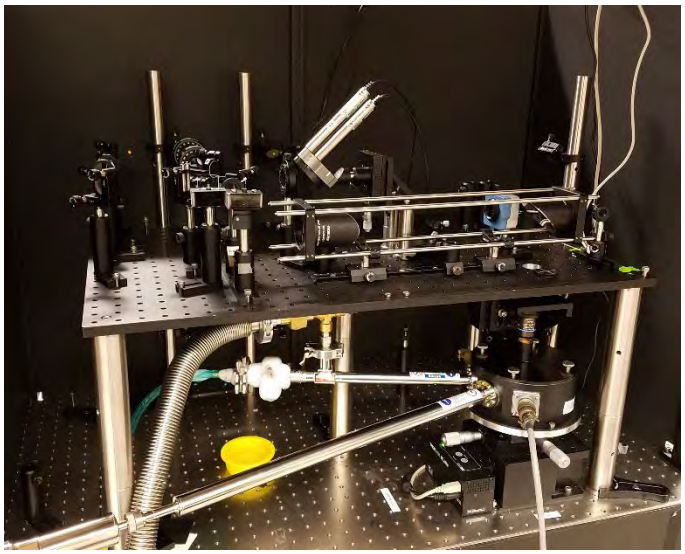

Figure 5. Experimental setup for valley lifetime.

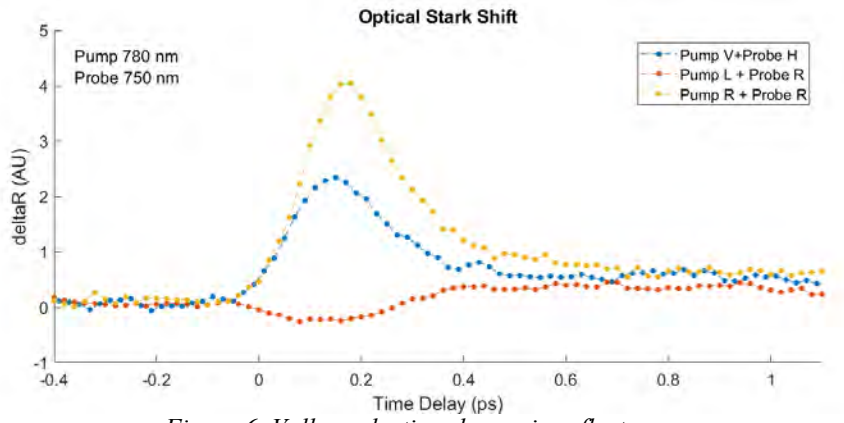

Figure 6. Valley-selective change in reflectance

This is a useable but nevertheless fairly short lifetime for practical purposes. The Gedik group is continuing to work on ways to increase valley lifetime by reducing substrate and environmental interactions using hBN capping layers above and below the monolayer WS_2. Additionally, they are evaluating heterostructures of WS_2 and WSe_2 to study the valley lifetime of interlayer excitons, which should be substantially longer due to greater physical separation between the electron and hole.

From the magnitude of the Stark shift measured and the experimental laser field intensity, an effective exciton dipole moment of 50 Debye is estimated.

2.2 ARBITRARY VALLEY STATE INITIALIZATION

Though we have focused on particles in the K and K′ states initialized by circularly polarized light, it should be possible to generate arbitrary superpositions of these states by linear or elliptically polarized states. Creating and manipulating states at any location on the Bloch sphere is a requirement for universal gate-based quantum computing. For classical computing, it may be very convenient to operate on states that are linearly polarized, as these states possess a static dipole moment and thus may be more easily operated upon by external fields to enable gate operations and information transport.

It has been well established that the K and K' valley states can be selectively initialized with σ+ and σ- excitation. Since linearly polarized light is a coherent superposition of σ+ and σ-, linearly polarized photons should initialize a coherent superposition of K and K', i.e., states on the equator of the Bloch sphere. A few linearly polarized photoluminescence experiments have been consistent with this assertion. However, single-point experiments that compare the PL intensity in just two polarizations are not entirely convincing as systematic errors may bias the measured polarization. This is particularly important as we explore the persistence of valley effects at room temperature where the valley polarization may be much less than one. Here we explore the creation of arbitrary superposition states by rotating the excitation through more than one complete revolution around the Poincaré sphere showing that the measured PL is

consistent with initialization of any valley polarized state from the poles of the Bloch sphere through several elliptically polarized states, to the equator, and then back again. To confirm that our results are not artifacts of systematic polarization biases, we quantitatively correct our measurements with simultaneous polarized Raman spectroscopy of the underlying silicon substrate.

Photoluminescence polarization is defined as

$$P_+ = \frac{I_+ - I_-}{I_+ + I_-}$$

$$P_- = \frac{I_- - I_+}{I_+ + I_-}$$

where P_+ indicates σ^+ excitation, P_- indicates σ^- excitation, I_+ is the intensity of the σ^+ component of the photoluminescence, and I_- is the intensity of the σ^- component of the photoluminescence. In principle, $P_+ = P_-$, but experimentally that is not always observed. Photoluminescence polarization has been measured for all four of the canonical transition metal dichalcogenides: MoS_2, $MoSe_2$, WS_2, and WSe_2. However, for each material, the reported results span a wide range from a few percent polarization to nearly 100% polarization. The variation is attributable to differences in sample quality, experimental conditions, and instrumentation errors. To reduce variation caused by inconsistent technique, we propose a method to correct raw polarized photoluminescence data to account for experimental non-idealities in the incident and detection light paths. We then demonstrate use of this method to measure small differences in room temperature valley polarization across spatially resolved 2D images.

To convincingly demonstrate that the polarization of the emitted photoluminescence is highly correlated to that of the incident excitation source, it is critical that both be known with high confidence. Polarization-resolved measurements at arbitrary angles can be difficult as optical elements, such as mirrors, do not perfectly persevere polarization at all angles of incidence and across the entire wavelength range of interests. To correct for systematic errors, we measure polarization resolved Raman scattering from the underlying silicon wafer, acquired simultaneously with the photoluminescence from the MoS_2 film. The Raman matrices for crystalline silicon are well known and the scattering intensity as a function of incident laser polarization for the first-order Raman mode can be easily calculated. Since the incident and emitted light for the Raman scattering and photoluminescence follow the same optical path, any experimentally measured deviation from the expected Raman signal can be applied as a correction to the polarization-resolved photoluminescence. This method is expected to be general for any material that can be grown on or transferred to a silicon substrate.

The experimental system is shown in Figure 7. A Renishaw InVia Raman microscope is used for all photoluminescence and Raman measurements. The microscope is coupled to a Montana Instruments Cryostation 2 for all measurements below room temperature. A 632.8 nm HeNe laser is used for excitation because it is close to the MoS_2 A exciton transition. MoS_2 samples were grown by CVD on SiO_2/Si(100) substrates.

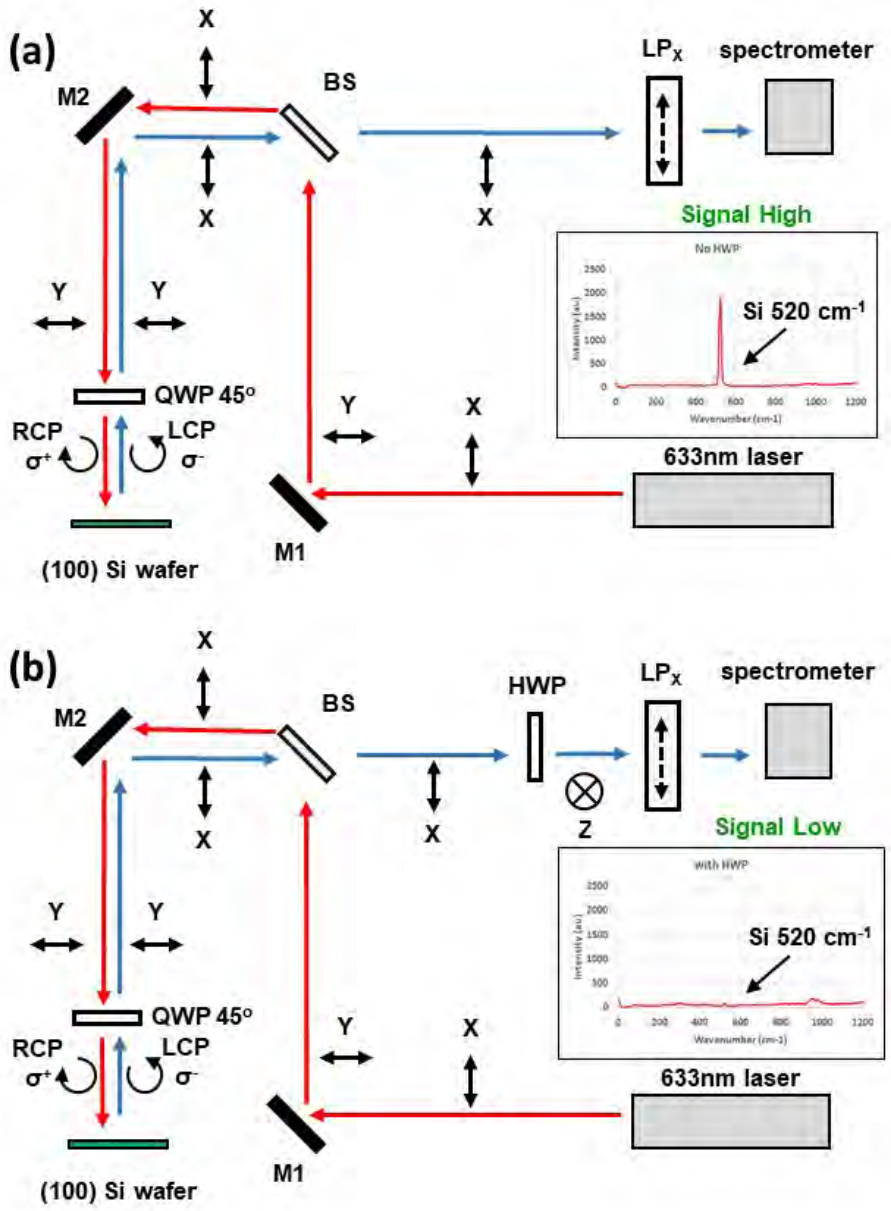

Figure 7. Experimental setup for polarization measurements: (a) measurement configuration for σ- detection, and (b) measurement configuration for σ+ detection.

Silicon wafers with or without MoS_2 were oriented such that the [010] direction was aligned with the Y-axis of our coordinate system (as defined in Figure 7) and the [001] direction was aligned with the Z-axis. The X-axis is normal to the (100) surface. This orientation allows for convenient use of the usual

silicon Raman matrices without need for coordinate transformation. In a typical experiment, the laser linear polarizer is rotated through 260° (limited by the motorized mounts) and data are collected with and without the HWP in place to collect the two orthogonally polarized components.

A 3×3 matrix Jones formalism is used to describe the system. For the experimental system shown in Figure 7, the measured Raman scattering light intensity is given by

$$I = I_o C \sum_j | \langle \boldsymbol{e_s} | \boldsymbol{HWP} | \boldsymbol{BS} | \boldsymbol{M2} | \boldsymbol{QWP} | \boldsymbol{R_j} | \boldsymbol{QWP} | \boldsymbol{M2} | \boldsymbol{BS} | \boldsymbol{M1} | \boldsymbol{e_i} \rangle |^2$$

where I_o is the laser intensity and C is a constant that accounts for Raman cross section and optical losses. e_s, *HWP*, *QWP*, *BS*, *M2*, *M1*, and e_i are the matrices for the analyzing linear polarizer, half wave plate, quarter wave plate, beam splitter, mirrors, and laser linear polarizer. R_j are the Raman matrices. Three Raman matrices contribute to the first-order Raman mode (F_{2g}) in silicon at 520 cm^{-1}.

$$\boldsymbol{R_x} = \begin{bmatrix} 0 & 0 & 0 \\ 0 & 0 & d \\ 0 & d & 0 \end{bmatrix} \qquad \boldsymbol{R_y} = \begin{bmatrix} 0 & 0 & d \\ 0 & 0 & 0 \\ d & 0 & 0 \end{bmatrix} \qquad \boldsymbol{R_z} = \begin{bmatrix} 0 & d & 0 \\ d & 0 & 0 \\ 0 & 0 & 0 \end{bmatrix}$$

The broad Raman feature in the silicon spectrum at 950–1000 cm^{-1} is due to the second-order modes, with scattering matrices

$$\boldsymbol{R_1}(\boldsymbol{A_{1g}}) = \begin{bmatrix} a & 0 & 0 \\ 0 & a & 0 \\ 0 & 0 & a \end{bmatrix} \qquad \boldsymbol{R_2}(\boldsymbol{E_{g1}}) = \begin{bmatrix} -b & 0 & 0 \\ 0 & -b & 0 \\ 0 & 0 & 2b \end{bmatrix} \qquad \boldsymbol{R_3}(\boldsymbol{E_{g2}}) = \begin{bmatrix} \sqrt{3}b & 0 & 0 \\ 0 & -\sqrt{3}b & 0 \\ 0 & 0 & 0 \end{bmatrix}$$

From these equations, the expected Raman signal intensities can be calculated for any orientation of the optical elements (via the Jones matrices) or silicon crystal orientation (by coordinate transformation of the Raman matrices).

The normalized Raman scattering signal intensity was measured as a function of laser angle. Figure 8a shows a polar plot of the two orthogonal components of the signal measured by inserting or removing a half wave plate to rotate the scattered light by 90°. The model prediction described above is shown as solid lines. Figure 8b shows the lack of fit between the collected data and the model. The residuals are less than 5% and represent the systematic polarization distortions. We correct the subsequent measured PL intensities at every laser excitation angle using the data in Figure 8b. We estimate the residual error in the PL measurements due to systematic distortions to be less than 2%.

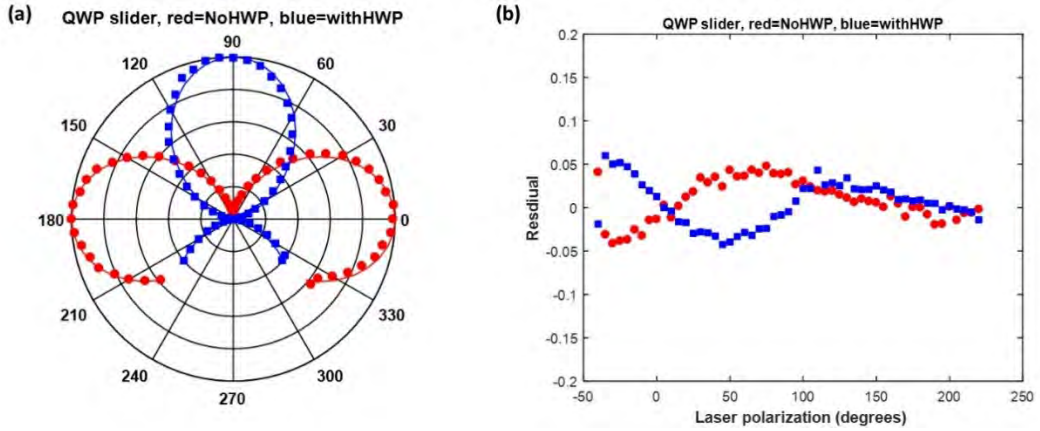

Figure 8. Circularly polarized Si Raman measurements: (a) first-order Si Raman intensity as a function of laser polarization angle—blue squares = σ+ detection, red squares = σ- detection; (b) difference between experimental data and model calculation.

Figure 9 shows the combined photoluminescence and Raman spectra from a monolayer MoS_2 sample on a SiO_2/Si wafer under σ+/σ+ and σ+/σ- excitation/measurement conditions. The Raman modes of the Si substrate and the MoS_2 are discernable. Note that the Si Raman signal is maximum in the σ+/σ- and σ-/σ+ configurations and minimum in the σ+/σ+ and σ-/σ- configurations, which is in agreement with the model. Though Raman modes of MoS_2 are present, though we chose not to use this signal for polarization assessment as it is difficult to deterministically align the MoS_2 crystal orientation in the system.

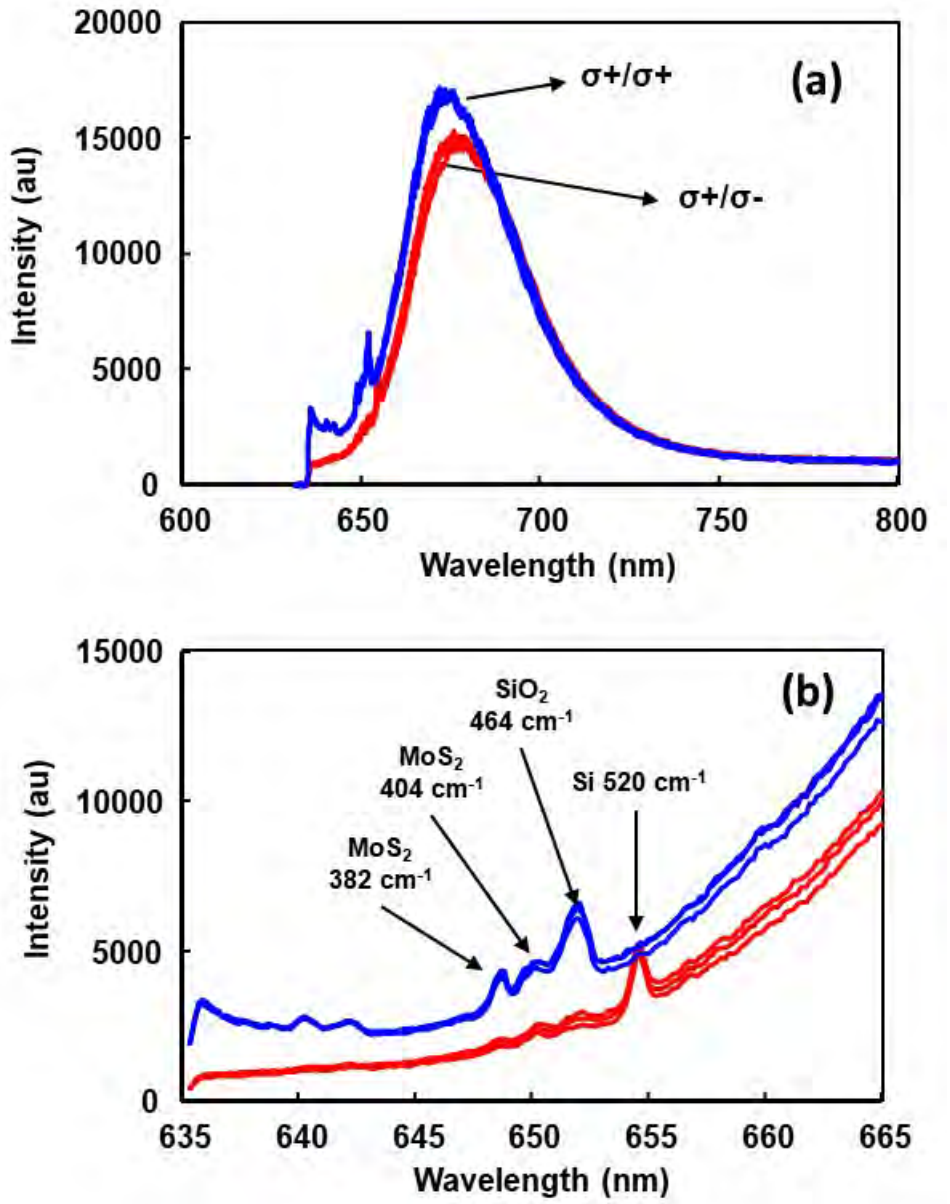

Figure 9. Simultaneously acquired MoS_2 PL and Si Raman: (a) spectra with σ+ excitation and detection of σ+ PL (blue) and σ- PL (red); (b) expanded view of data in (a) showing Raman peaks.

The MoS_2 σ- PL component as a function of laser angle is shown in Figure 10. The PL is rotated by 90° compared to the Raman scattering signal. In this case, we replace R_j with a matrix PL representing PL emission, which in the case of near-resonant excitation is simply the identity matrix.

As expected, the σ- PL is emission is a maximum when the excitation is σ- and in a minimum when the excitation is σ+. Importantly, the σ- PL measurement agrees with the proportion of the excitation that is σ-. This is consistent with the generation of valley superposition states at arbitrary elliptical polarization. Unlike the Raman signal, the PL intensity does not go to zero due to thermalization of excitons between the two valleys resulting in a background contribution PL_u, which is independent of the incident polarization. The normalized model becomes

$$I = PL_U + PL_V \sum_j |\langle e_s | \boldsymbol{HWP} | \boldsymbol{BS} | \boldsymbol{M2} | \boldsymbol{QWP} | \boldsymbol{PL} | \boldsymbol{QWP} | \boldsymbol{M2} | \boldsymbol{BS} | \boldsymbol{M1} | e_i \rangle|^2$$

Fitting this equation to the data in Figure 10 suggests a room temperature valley polarization of 10% in this sample of CVD MoS_2.

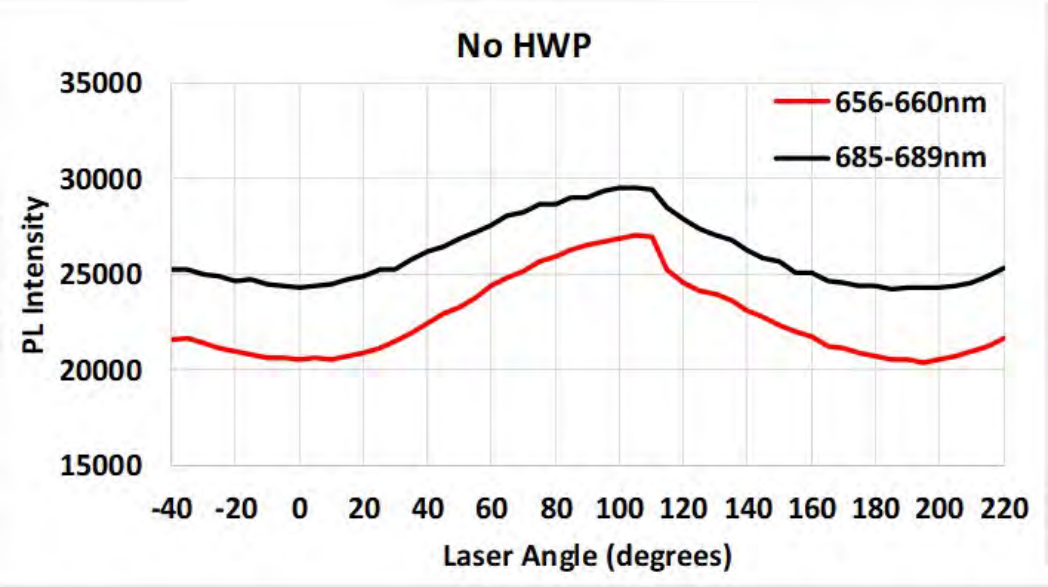

Figure 10. σ- PL emission in two spectral bands.

2.3 VALLEY POLARIZATION IMAGING

For any practical classical information processing application, devices must support integration at densities comparable to conventional microelectronics (currently tens of devices per square micron). For consistent device-to-device operation, valleytronic effects must be uniform from the sub-micron scale to the length scale of the fabricated microchip (~1 cm). In this section, we explore the spatial homogeneity of valley initialization from the 0.5 μm scale to the 10 μm scale, limited by the wavelength of excitation and the size of our MoS_2 crystalline domains, respectively. Here we consider the spatial uniformity of CVD monolayer MoS_2 samples grown by Jing Kong's group in the MIT Department of Materials Science.

Valley polarization measurements to date have focused on single-point measurements within a crystalline domain or averaged across a sample. Here we present maps of valley polarization acquired with submicron resolution to investigate spatially inhomogeneous effects. A valley polarization map of a single MoS2 crystal in the σ+/σ+ excitation/measurement configuration is given in Figure 11. The mean valley polarization of this crystal is 10%. The standard deviation across the crystal is 3%, though the distribution is not completely random. The valleytronic properties are expected to be influenced by crystal defects, edges, and domain boundaries.

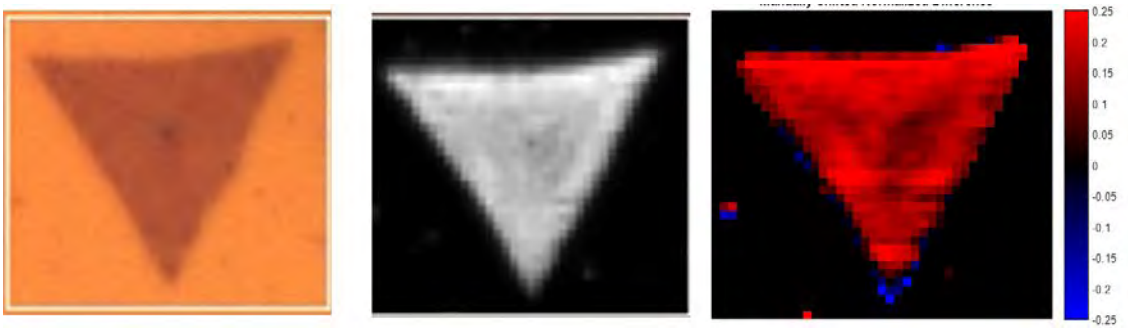

Figure 11. Images of a monolayer MoS_2 single crystal: (left) white light optical image, (middle) PL intensity map, and (right) P+ polarization map.

The polarization map of a non-triangular monolayer single crystal of MoS_2 is shown in Figure 12. From the PL image, it appears this crystal is the result of several smaller triangles that merged together as they grew, as there is evidence of lower PL along grain boundaries (Figure 12, middle). The valley polarization image does not resolve a decrease in valley polarization at these boundaries (Figure 12, right); however, the overall valley polarization is lower at 5%. This suggests that the presence of grain boundaries has an adverse impact on the valley properties.

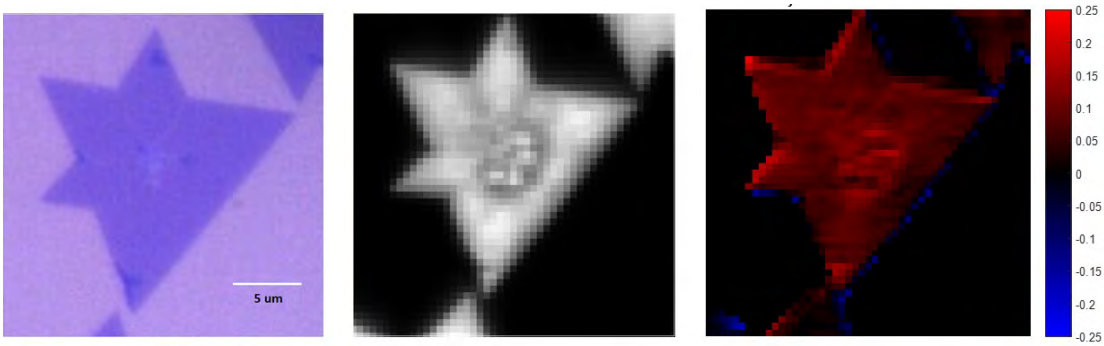

Figure 12. Images of merged monolayer MoS_2 single crystals: (left) white light optical image, (middle) PL intensity map, and (right) P+ polarization map

Figure 13 shows the valley polarization of a completely merged area. Based on the MoS_2 Raman peaks, this area is mostly monolayer MoS_2, but the single domains have grown together into a continuous film. The PL in Figure 13 (middle) shows distinct areas of low PL, which we suspect are regions where the domains have overgrown one another and represent bilayer regions. This is supported by the valley polarization map in Figure 13 (right), which shows zero valley polarization in the overlapped regions, consistent with bilayer MoS_2.

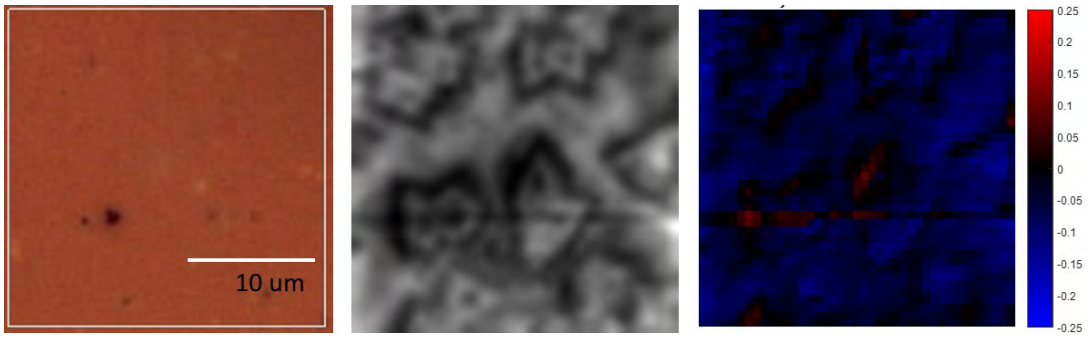

Figure 13. Images of merged MoS_2 crystals: (left) white light optical image, (middle) PL intensity map, and (right) P+ polarization map.

2.4 EFFECT OF TEMPERATURE

The main application of this work is general purpose computing that will by necessity be performed at room temperature. However, there may be niche applications for cryogenic computing, so we evaluated the valley polarization behavior at cryogenic temperatures as well. As shown in Figure 14, the valley polarization increases from 10% at room temperature to 25% at 77 K. Even at 77 K, however, there is distinct non-uniformity in valley polarization across the crystal.

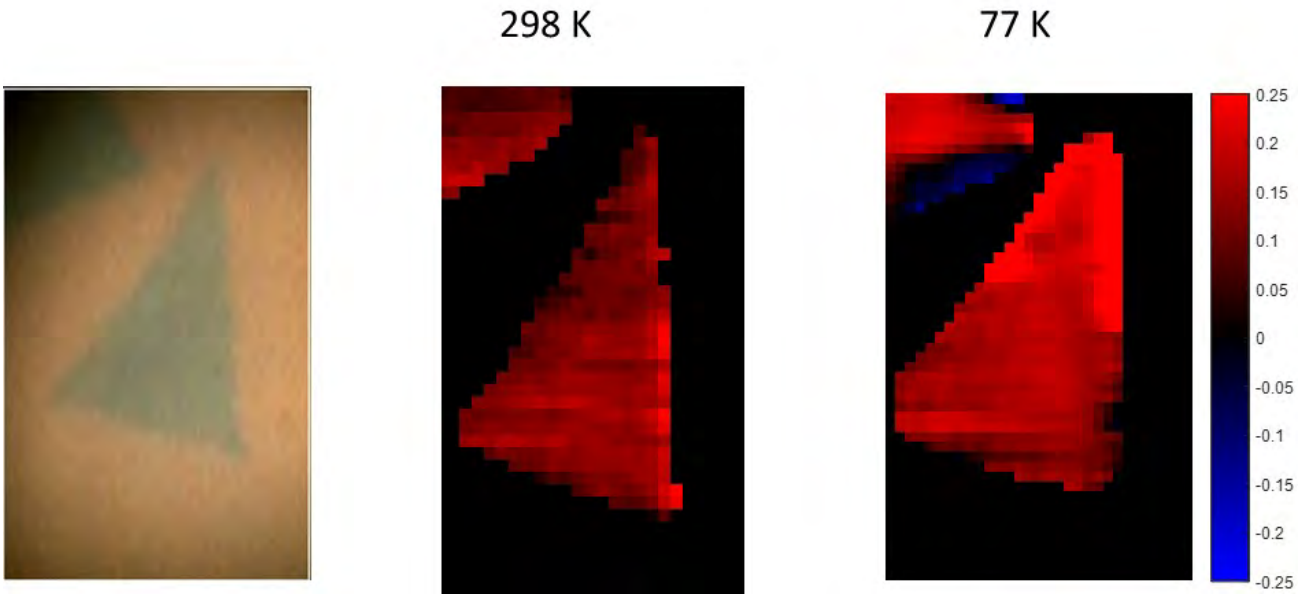

Figure 14. Images of a monolayer MoS_2 single crystal: (left) white light optical image, (middle) P_+ polarization map at room temperature, and (right) P_+ polarization map at 77 K.

This page intentionally left blank.

3. VALLEYTRONIC LOGIC PERFORMANCE ANALYSIS

Using the above data, we can begin a PPA analysis of a valleytronic logic gate. Consider a notional CNOT gate that is logically equivalent to a reversible XOR gate with two inputs and two outputs (Figure 15). The inputs and outputs are optical. The information carrier is a valley exciton where the momentum index of the exciton represents the 0 or 1 state. One input (Y) is an exciton initialized as 0 or 1. The other input is an optical control pulse (X): if present (1), the control pulse rotates the exciton input from the 0 state to the 1 state. If the control pulse is not present (0), the exciton is unchanged. Readout occurs optically by measuring the chirality of the photoluminescence photon emitted when the exciton recombines.

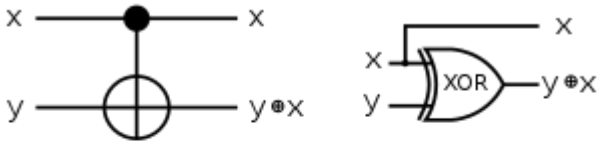

input		output	
x	y	x	y+x
|0⟩	|0⟩	|0⟩	|0⟩
|0⟩	|1⟩	|0⟩	|1⟩
|1⟩	|0⟩	|1⟩	|1⟩
|1⟩	|1⟩	|1⟩	|0⟩

input		output	
x	**y**	**x**	**y+x**
0	0	0	0
0	1	0	1
1	0	1	1
1	1	1	0

Figure 15. CNOT gate. From Wikipedia.

We will calculate the energy cost of an inverting gate operation, X=1. Initializing the input Y will require energy E_i, given by

$$E_i = \frac{n_{exc}E_g}{f_i} = \frac{n_{exc}E_g}{\alpha P}$$

where n_{exc} is the number of excitons required to generate an output well above the noise floor, E_g is the band gap of the TMD material, f_i is the initialization efficiency, α is the absolute absorption of the TMD, and P is the polarization fidelity.

State evolution is performed by applying a control pulse that rotates state X through a phase evolution of $-i\omega t$. For a phase shift $\Delta\varphi=\pi/2$ within a time τ, we need to induce an energy splitting between the 0 and 1 states:

$$\Delta E = \hbar\omega = \hbar\frac{\Delta\varphi}{\tau}$$

As an example, using the measured valley lifetime of 0.2 ps for τ, the required energy splitting is 5.16 meV. The electric field of the laser control pulse can be related to the energy splitting by

$$\Delta E = \hat{d} \cdot \vec{E} = d|E|$$

where f_c is the control pulse efficiency, $\hat{d}$ is effective electric dipole of the exciton, $\vec{E}$ is the laser field, and for the right-hand expression, the laser polarization has been aligned in the same plane as the exciton dipole. Laser pulse energy is

$$P_L\tau = I_L A\tau = \left(\frac{c\varepsilon_o}{2}|E|^2\right)A\tau$$

where P_L is the laser power, I_L is the laser intensity, and A is the illuminated area. Substituting for $|E|$, we find get an expression for the control pulse energy

$$E_c = A\tau\frac{c\varepsilon_o}{2}\left(\frac{\Delta E}{d}\right)^2 = A\frac{c\varepsilon_o}{2\tau}\left(\frac{\pi\hbar}{2d}\right)^2$$

From this equation, we see that the control pulse energy decreases with valley lifetime and is quadradically sensitive to the effective exciton dipole moment.

For the purposes of this calculation, we will assume that the output exciton converts to a photon with unity yield, which is then routed to a photodiode and a charge storage register. Readout efficiency f_r is a function of the waveguide attenuation α_W and waveguide length L:

$$f_r = 10^{-\alpha_w L}$$

The total energy cost of the inverting gate operation is now given by

$$E_{tot} = \frac{1}{f_r}(E_i + E_c) = \frac{1}{f_r}\left(\frac{n_{exc}E_g}{\alpha P} + A\frac{c\varepsilon_o}{2\tau}\left(\frac{\pi\hbar}{2d}\right)^2\right)$$

Using the data from Section 2 and some literature values, one can evaluate this expression. We take, α_w = 1 dB/cm, L = 10 μm, n_{exc} = 10, E_g = 1.8 eV, α = 0.01, P = 10%, A = 1 μm^2, τ = 0.4 ps, and d = 50 Debye. The energy per CNOT operation is 6.112 fJ, and is nearly equally split between the initialization and control pulse energy demands. By comparison, the active switching energy of a CMOS transistor is approximately equal to CV^2, which for a six-transistor XOR gate in a 0.9V 14 nm technology is equal to ~0.053 fJ.

4. SUMMARY

Foundational measurements to inform valleytronic computing applications were performed on monolayer MoS_2 at MIT LL and on WS_2 at MIT campus. At MIT LL, a technique to obtain precise Raman-corrected valley polarization measurements was developed. We determined with a relatively high degree of precision that valley state initialization is robust not just at the K and K' points, but at any superposition states around the Bloch sphere. In addition, we are able to perform accurate valley polarization imaging at the micron scale, which we believe to be the first measurements of their kind at both room temperature and at cryogenic temperatures. From these measurements, we derive: 1) the appropriate length scale that can be supported by future valleytronic devices, and 2) a practical value for valley polarization. On campus, ultrafast valley polarization spectroscopy and Optical Stark Effect were performed on monolayer WS_2. From these measurements, we derive the timescale for valley logic operations and the effective dipole moment of the excitons.

We derived an expression for the switching energy of a logical valleytronic CNOT gate. Using the above-measured parameters, we estimate that using currently available technology, the energy cost will be approximately 6.1 fJ per valleytronic logic gate operation. This is more than 100× larger than the switching cost of a commercial 14 nm CMOS logic gate with similar functionality. At the current state of the art, valleytronic logic is not competitive with CMOS power consumption.

The development of valleytronic logic devices is still in its infancy, however. Key parameters in the device performance model include the effective dipole moment, polarization fidelity, and the valley lifetime. Orders of magnitude improvement are possible in the dipole moment and valley lifetime, and as much as a 10× in valley polarization. There are several active areas of research to improve those parameters, including: heterostructures of TMD layers to allow robust interlayer excitons, improved synthesis techniques to reduce valley scattering centers, and suspended structures to remove substrate coupling. At this time, it is recommended to continue following the field for improvements in the key material parameters identified in this work.

This page intentionally left blank.

5. REFERENCES AND PRESENTATIONS

[1] S.A. Vitale, D. Nezich, J.O. Varghese, P. Kim, N. Gedik, P. Jarillo-Herrero, D. Xiao, and M. Rothschild, *Small* 2018, 14, 1801483.

[2] D. Xiao, G.-B. Liu, W. Feng, X. Xu, W. Yao, Physical Review Letters, 108, 196802, 2012.

[3] X. Xu, W. Yao, D. Xiao, T.F. Heinz, *Nature Physics* 2014, *10*, 343.

[4] D. Xiao, G.-B. Liu, W. Feng, X. Xu, W. Yao, *Physical Review Letters* 2012, *108*.

[5] D. Xiao, W. Yao, Q. Niu, *Physical Review Letters* 2007, *99*.

[6] T. Cao, G. Wang, W. Han, H. Ye, C. Zhu, J. Shi, Q. Niu, P. Tan, E. Wang, B. Liu, J. Feng, *Nature Communications* 2012, *3*, 887.

[7] K.F. Mak, K. He, J. Shan, T.F. Heinz, *Nature Nanotechnology* 2012, *7*, 494.

[8] H. Zeng, J. Dai, W. Yao, D. Xiao, X. Cui, *Nature Nanotechnology* 2012, *7*, 490.

[9] K.F. Mak, K.L. McGill, J. Park, P.L. McEuen, *Science* 2014, *344*, 1489.

[10] S.A. Vitale, "Valleytronic Information Processing and Applications," 2019 NSF/DOE/AFOSR Quantum Science Summer School, Penn State University, June 2019.

[11] M.B. Yilmaz, E. Ergecen, N.P. Wilson, J. Varghese, S. Vitale, X. Xu, N. Gedik, "Ultrafast Dynamics of Excitonic Rydberg Series in Single Layer WSe_2," APS March Meeting, Boston, MA, March 2019.

[12] S.A. Vitale, J.O. Varghese, D.A. Nezich, M. Rothschild, "A universal method for measuring valleytronic quality of 2D materials using conventional Raman spectroscopy," AVS 64th International Symposium, Long Beach, CA, November 2018.

[13] S.A. Vitale, "Valleytronics for Information Processing," Enabling Quantum Leap: Convergent Approach to the Challenges of Moore's Law Workshop, Georgetown University, November 2018.

This page intentionally left blank.